SOLAR-TYPE ECLIPSING BINARY KIC 4832197: PHYSICAL PROPERTIES AND INTRINSIC VARIABILITY OF THE COMPONENTS

O. Özdarcan, H. A. Dal, and E. Yoldaş

Department of Astronomy and Space Sciences, Faculty of Science, Ege University, İzmir, Turkey.

ABSTRACT

Comprehensive analysis of optical spectroscopy and space photometry of the solar type eclipsing binary system KIC 4832197 is presented. The system is composed of F7V + F9V components with masses of $M_1 = 1.16 \pm 0.12$ M$_\odot$, $M_2 = 1.07 \pm 0.10$ M$_\odot$ and radii of $R_1 = 1.26 \pm 0.04$ R$_\odot$, $R_2 = 1.03 \pm 0.03$ R$_\odot$. The position of the components on the Log T_{eff} − Log $L/L_\odot$ plane suggests an age of 2.8 ± 0.8 Gyr for the system. Inspection of out-of-eclipse brightness in time reveals a wave-like variability pattern, whose amplitude and shape quickly change on order of days. Frequency analysis of this variability results in two significant peaks in the amplitude spectrum, which are interpreted as rotational modulation of spots on the components. Assuming both spots are on the same component, a lower limit for the differential rotation coefficient is computed as $k = 0.12$, which is weaker compared to the solar value of $k_\odot = 0.189$.

RESUMEN

Presentamos un análisis de la espectroscopía óptica y fotometría de la binaria eclipsante tipo solar KIC 4832197. El sistema se compone de dos estrellas F7V + F9V, con masas de $M_1 = 1.16 \pm 0.12$ M$_\odot$, $M_2 = 1.07 \pm 0.10$ M$_\odot$ y radios de $R_1 = 1.26 \pm 0.04$ R$_\odot$, $R_2 = 1.03 \pm 0.03$ R$_\odot$. La posición de las componentes en el plano Log T_{eff} − Log $L/L_\odot$ sugiere una edad de 2.8 ± 0.8 Gyr. La inspección del brillo fuera de eclipse revela una variabilidad ondulatoria, cuya amplitud y forma cambian rápidamente, en días. El análisis de la frecuencia de esta variabilidad arroja dos picos significativos en el espectro de amplitud, que se interpretan como una modulación rotacional de manchas en las componentes. Si suponemos que ambas manchas están en una de las componentes, calculamos un límite inferior para el coeficiente de rotación diferencial de $k = 0.12$, más pequeño que el valor solar, que es $k_\odot = 0.189$.

Key Words: binaries: eclipsing — stars: activity — stars: fundamental parameters — stars: individual: KIC 4832197

1. INTRODUCTION

Observed rotational modulation of brightness in a light curve of a solar-type star is interpreted as a strong photometric evidence of cool star spots on the stellar surface, which co-rotate with the surface. These spots might emerge in various locations on the surface of the star as a manifestation of the magnetic activity, which is commonly observed among solar-type stars. Such a light curve allows one to trace the temporal and spatial evolution of spots, as well as to determine the photometric period of the star. Finding the photometric period of a single star is crucial because that period can be considered as the rotation period the star. In the case of binary stars, it is possible to determine the photometric and orbital period separately. If the components of the binary system are solar-type stars, then a comparison between the photometric period and the orbital period provides hints on the surface differential rotation, which is one of the key parameter that drives the dynamo mechanism in stellar interiors.

Until the era of very high precision space photometry, photometric studies of the magnetic activity of solar-type stars had relied on long-term time-series

photometry obtained from dedicated ground-based telescopes (Henry & Eaton 1995; Strassmeier et al. 1997; Rodonò et al. 2001) or on all sky surveys (Pojmanski 1997; Kochanek et al. 2017). These sources provided photometric data with an uncertainty of a few percent of a magnitude (rarely at milimag level; e.g. Henry & Eaton 1995) and enabled to trace the short and long-term magnetic activity behaviour of solar-type stars in terms of mean brightness, light curve amplitude and photometric period.

After entering the era of groundbreaking space photometry, astronomers had extremely high precision photometric data obtained in a wide wavelength range. Especially, the *Kepler* space telescope (Borucki et al. 2010; Howell et al. 2014) reached a photometric precision down to a few tens of part-per-million. Such a precision not only enabled to detect a planetary transit in a light curve, which was the primary mission of the *Kepler* space telescope, but also sub-millimag amplitude variability of stars. In the case of magnetic activity of solar-type stars, such precision allowed detection of very small amplitude rotational modulation of brightness, which could not be distinguished in ground-based photometry due to the typical observational scatter of a few per-cent of a magnitude. In addition to its very high precision, *Kepler* photometry spans over four years without any considerable time gap, which enables one to trace low amplitude photometric signs of magnetic activity of solar-type stars. All these properties encouraged research for more detailed and comprehensive photometric studies of stellar flares and differential rotation of large sample of stars (Balona 2015; Reinhold & Gizon 2015) or of individual targets, (particularly eclipsing binaries; Yoldaş & Dal 2021; Özdarcan et al. 2018). In some cases, *Kepler* photometry revealed effects of two separate variability mechanisms, (e.g. pulsation and cool spot activity), in eclipsing binary system (see, e.g., Özdarcan & Dal 2017).

In this study, we present a comprehensive analysis of a solar-type eclipsing binary system KIC 4832197. Our analysis is based on ground-based medium resolution optical spectroscopy and *Kepler* photometry. KIC 4832197 draws attention with its very shallow eclipse depths in its light curve and its remarkable out-of-eclipse variability with an amplitude that is comparable to the eclipse depths. Neither eclipses nor out-of-eclipse variability of the system were discovered until the advent of very high precision *Kepler* photometry. The system was included in the planet candidate catalogue due to its shallow eclipse depths (Coughlin et al. 2016). How-

ever, no confirmed exoplanet in this system has been reported so far. KIC 4832197 appeared as a late A spectral type star according to Tycho-2 measurements ($B - V = 0^\text{m}202 \pm 0^\text{m}111$, Høg et al. 2000). On the other hand, more recent and precise broadband UBV colours and magnitudes of the system are $V = 11^\text{m}673 \pm 0^\text{m}018$, $B - V = 0^\text{m}496 \pm 0^\text{m}030$ and $U - B = -0^\text{m}002 \pm 0^\text{m}032$ (Everett et al. 2012), which indicate an F7 spectral type for the system (Gray 2005).

Remarkable out-of-eclipse variability may indicate cool spot activity or pulsations on one or both components. Furthermore, shallow eclipses may indicate a possible third light, which may reduce eclipse amplitudes in the light curve depending on its contribution to the total light of the system. All these properties of KIC 4832197 are promising not only for testing stellar evolution models, but also for further studies on the variability mechanism currently occurring in one or both components. Analysis of very high precision *Kepler* photometry is excellent for such studies.

In this context, we combine ground-based optical spectroscopy and space photometry to determine the physical properties of the system and its evolutionary status. We further analyse brightness variability at out-of-eclipse phases, which can shed light into the current variability mechanism on the components of KIC 4832197. We organize the remaining parts of our study as follows. We describe the observational data and reduction in the next section. Section 3 includes light time variation analysis, spectroscopic and photometric modelling of the system, including atmospheric parameter estimation of each component, spectroscopic orbit of the system and light curve analysis. In the last section, we summarize our findings and discuss our results.

2. DATA

2.1. *Spectroscopy*

Medium resolution optical spectra of KIC 4832197 were obtained at TÜBİTAK National Observatory (TNO) with the 1.5 m Russian-Turkish telescope and the Turkish Faint Object Spectrograph Camera (TFOSC[1]). An Andor DW436-BV 2048×2048 pixels CCD camera with a pixel size of $13.5 \times 13.5 \ \mu m^2$ was used, which allows recording optical spectra between 3900 – 9100 Å in 11 échelle orders. This instrumental set-up provided an average resolution of $R = \lambda/\Delta\lambda = 2700 \pm 500$ around the $\lambda = 5500$ Å wavelength region. Observations

---

[1]https://tug.tubitak.gov.tr/en/teleskoplar/rtt150-telescope-0

were carried out on eight nights between July 2014 and April 2017. Ten spectra were recorded in total.

Conventional procedures for reducing échelle spectrum images were followed. These steps are applied under IRAF environment[2] and start with the removal of bias level and continue by division of bias-removed object and calibration lamp images by a normalized flat-field image. Then, scattered light correction and cosmic rays removal steps are applied to the bias and flat-field corrected images. Finally, object and calibration lamp spectra are extracted from the échelle orders. Wavelength calibration of the extracted object spectra is done by using a Fe-Ar calibration lamp spectrum recorded on the same observing night. After completing standard reduction steps, all object spectra were normalized to unity by applying 4th or 5th order cubic spline functions.

2.2. *Kepler Photometry*

Very high precision space photometry of KIC 4832197 was obtained by *Kepler* spacecraft. The spacecraft recorded images in 6.02 second exposure times with 0.52 second read-out times in a broad wavelength range between 4100 Å and 9100 Å (Gilliland et al. 2010). The broad wavelength range allows to record more photons in a single exposure, which increases precision, at the expense of losing colour information. From the recorded images, two data sets were created depending on two separate integration times; 58.9 second (short cadence data) and 29.4 minute (long cadence data). These integrations were grouped as separate data sets, where each set covered approximately three months, called quarters, except the first quarter, which covered ten days of commissioning phase and is called quarter zero (Q0). During operation of the spacecraft over 4 years (between 2009 and 2013) photometric data were collected for eighteen quarters in total (from Q0 to Q17). Continuous long cadence photometry obtained in each quarter is available for the majority of *Kepler* targets, including KIC 4832197. Long cadence photometry of KIC 4832197 for each quarter is obtained from Mikulski Archive for Space Telescopes (MAST). Prior to analyses, it is necessary to remove instrumental effects from the long cadence data. For each quarter, simple aperture photometry (SAP) fluxes are considered. These fluxes are de-trended as described in Slawson et al. (2011) and Prša et al. (2011). De-trended fluxes are then normalized to unity. The analysis and modelling process

is based on these normalized fluxes. We show the long cadence light curve of KIC 4832197 in Figure 1.

3. ANALYSIS

3.1. *Light Time Variations*

The first step of the analysis is to determine mid-eclipse times of KIC 4832197 for primary eclipses. In principle, mid-eclipse times can be determined straightforwardly by applying the Kwee - van Woerden method (Kwee & van Woerden 1956) to observations close by to mid-eclipse time. An alternative way is to fit a function to the observational data around the estimated mid-eclipse time and determine the extremum point of this function, which corresponds to the mid-eclipse time. These methods may work flawlessly for a light curve of an ordinary eclipsing binary, which shows symmetric eclipse light curves with respect to the mid-eclipse time and exhibits flat or slightly distorted maxima at out-of-eclipse phases. Such light curves indicate the absence of intrinsic variability for any of the component. Looking at Figure 1, one may easily notice the variable nature of the light curve. Because of the relatively short orbital period and integration time of long cadence data, a few data points can be found around the expected mid-eclipse time for a given orbital cycle. Combination of these two effects gives a complex shape to the light curve and makes the methods mentioned above unsuited for the precise determination of mid-eclipse times. In such cases, one of the most reliable ways is to find a best-fitting light curve model and then only adjust the mid-eclipse time of the primary minimum in the model for each cycle. We follow exactly this way for a precise determination of mid-eclipse times from long cadence data.

Actually, this is an iterated process, which starts by preparing a phase-folded light curve with initial light elements, i.e. an ephemeris reference time (T_0) and an orbital period (P), then continues by finding the best-fitting light curve model. In the case of KIC 4832197, initial T_0 and P values are adopted from the Kepler Eclipsing Binary Catalogue[3] (Prša et al. 2011; Slawson et al. 2011) given in equation 1:

$$T_0(\text{BJD}) = 2,454,954.965798 + 1^{\text{d}}8954655 \times E. \quad (1)$$

After finding the best-fitting light curve model, T_0 is adjusted for each orbital cycle separately, by keeping all other model parameters fixed. In this step, time-based long cadence data are considered,
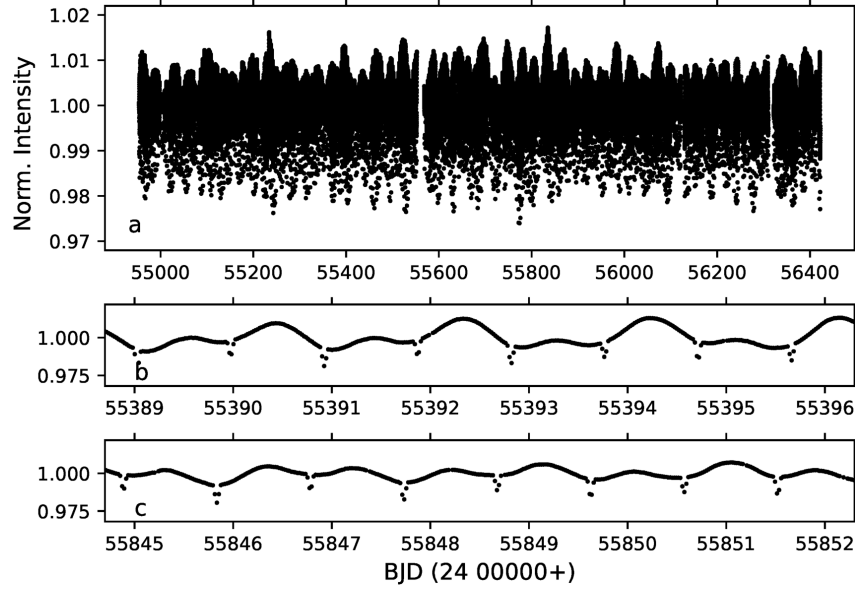

Fig. 1. In panel a the long cadence light curve of KIC 4832197 is shown. In panels b and c, different portions of the long cadence light curve are shown, where the shape of the light curve remarkably changes.

instead of phase-folded light curve. Thus, the mid-eclipse time of each orbital cycle can be determined precisely together with formal errors. Practical application of this method is done with the Wilson-Devinney code (see later sections for details). After determination of mid-eclipse times, a simple eclipse time variation (etv) diagram is constructed and linear corrections are determined and applied to both T_0 and P. Then the whole process is repeated by using the corrected T_0 and P. In most cases, two iterations are enough to obtain self consistent T_0, P, and light curve model parameters. The converged solution leads to the corrected light elements given in equation 2:

$$T_0(\text{BJD}) = 2,454,954.9661(2) + 1\overset{\text{d}}{.}8954650(4) \times E. \tag{2}$$

The numbers in parentheses are statistical uncertainties for the last digit of the corresponding parameter. These uncertainties are computed from a linear least squares fit. T_0 and P values given in equation 2 are adopted for further analyses and kept fixed. The resulting eclipse time variation diagram is shown in Figure 2. In the figure, an irregular undulating variation is noticeable among the scatter, with an approximate amplitude of $0\overset{\text{d}}{.}003$. Since that pattern does not repeat itself strictly over four years, it is not likely to be due to a possible third body. A more likely explanation of this pattern might be the out-of-eclipse variability of the system, which can be noticed in the b and c panels of Figure 1.
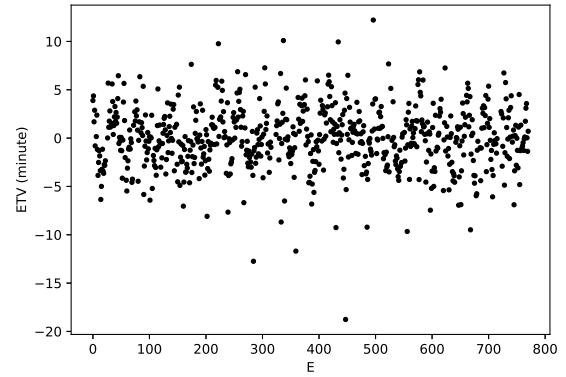

Fig. 2. ETV diagram for KIC 4832197.

3.2. Radial Velocities and Spectroscopic Orbit

The next step of our analysis is to determine radial velocities of each component from each observed spectrum and to model the spectroscopic orbit of the system. In order to determine radial velocities of the components, we use the optical spectrum of HD 184499 (T_{eff} = 5743, log g = 4.07; Prugniel et al. 2011) as a template spectrum, which was recorded with the same instrumental set-up on 20th August, 2014. Then, each observed spectrum of KIC 4832197 was cross-correlated with the spectrum of HD 184499 by following the method proposed by Tonry & Davis (1979). The practical application of this method used the *fxcor* task (Fitzpatrick 1993) under IRAF environment. All clear absorption lines (except strongly blended or very broad spectral lines) were considered in the 5th and 6th
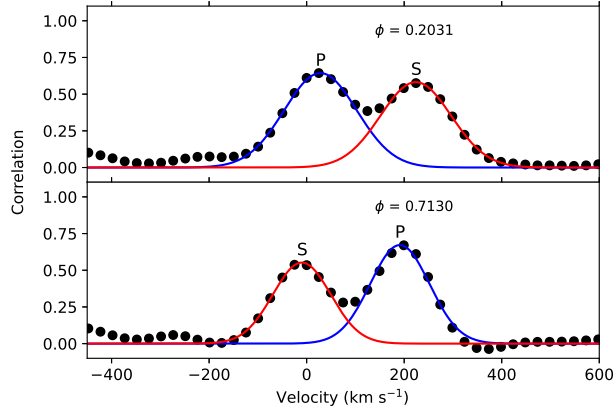
Fig. 3. Cross-correlation functions of two observed spectra recorded around orbital quadratures. P and S denote the primary and the secondary component, ϕ the orbital phase. The colour figure can be viewed online.

échelle orders, which cover a wavelength range between 4900 Å and 5700 Å. In this wavelength range, it was possible to detect strong signals of both components. We show cross-correlation functions of two spectra of KIC 4832197, recorded at two separate orbital quadratures, in Figure 3. The heliocentric radial velocities are tabulated in Table 1.

Preliminary inspection of the phase-folded light curve shows that the mid-primary and the mid-secondary eclipses precisely occur at 0.0 and 0.5 orbital phases, respectively. This finding strongly suggests a circular orbit. Therefore, the spectroscopic orbit of the system is determined assuming zero eccentricity (i.e. $e = 0$). In this case, the longitude of the periastron (ω) is undefined; thus the T_0 value found in the light time variation analysis step is adopted instead of the periastron passage time. T_0 and P values are kept fixed during the modelling, while radial velocity semi-amplitudes of the components (K_1 and K_2), center-of-mass velocity of the system (V_γ) are adjusted. Application of a linear least squares fitting method to the observed radial velocities results in the best-fitting spectroscopic orbit parameters tabulated in Table 2. The agreement between the observed radial velocities and their best-fitting model is shown in Figure 4.

3.3. *Spectral Type*

Medium resolution TFOSC spectra allow us to determine spectral types and global atmospheric parameters for each component of KIC 4832197. A spectrum recorded around any of the orbital quadrature is suitable for the atmospheric parameter determination of individual components, since the spectral lines of both components are often sufficiently
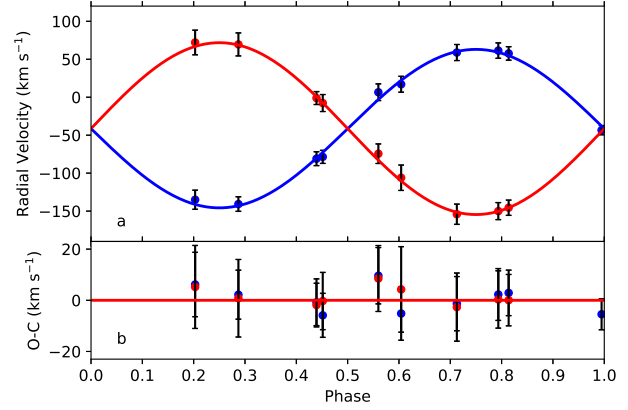

Fig. 4. Phase-folded radial velocities of the primary (blue) and the secondary (red) components are shown as filled circles. The best-fitting spectroscopic orbit model is over-plotted for each component as a continuous line. The colour figure can be viewed online.

separated from each other and can be distinguished at those orbital phases. This is observed in the TFOSC spectrum recorded on 30th July 2016, corresponding to 0.7130 orbital phase (see lower panel of Figure 3). Spectral types and atmospheric parameters are determined from this spectrum.

Determination of spectral types and atmospheric parameters is an iterated process, as in the case of determination of mid-eclipse times described in § 3.1. During the analysis, we fix the micro-turbulence velocity of each component at 2 km s^{-1}. Actually, analysing high resolution optical spectra it is possible to determine the micro-turbulence velocity and the [Fe/H] abundance simultaneously, via the Blackwell diagram (Blackwell & Shallis 1979). However, due to the insufficient resolution of TFOSC spectra, we were unable to do so. Instead, we implicitly assume a 2 km/s micro-turbulence velocity and fix this value during the analysis. Although there is no strict relation in the literature to estimate micro-turbulence velocities reliably, limited observational studies indicate that 2 km s^{-1} is appropriate for solar type stars (Landstreet et al. 2009).

It is possible to apply a constraint on the logarithm of gravity (log g) of the components. To do this, spectroscopic orbit model parameters are combined with preliminary light curve solution parameters. This step allows computation of the masses and radii of the components. Then, log g values are computed via the computed masses and radii of the components. Computed log g values are fixed in the spectral type analysis and effective temperatures of the components (T_{eff1} and T_{eff2}) are estimated together with overall metallicity ([Fe/H]). Then, the

TABLE 1

SUMMARY OF SPECTROSCOPIC OBSERVATIONS[*]

HJD (24 00000+)	Orbital Phase	Exposure time (s)	SNR	Primary		Secondary	
				V_r	σ	V_r	σ
56842.4581	0.7936	3200	120	61	10	-150	11
56842.4963	0.8138	3200	95	58	9	-146	10
56843.3937	0.2872	3200	90	-141	10	70	15
56887.3009	0.4516	3200	140	-79	9	-8	11
56887.5063	0.5599	3200	95	7	11	-74	13
56888.3307	0.9949	3200	120	-43	6	—	—
57592.3910	0.4395	3600	90	-81	9	-1	9
57600.4912	0.7130	3600	110	59	11	-154	13
57617.3447	0.6045	3600	90	17	10	-106	17
57853.5170	0.2031	2700	100	-135	13	72	16

[*]Along with the measured radial velocities and their corresponding standard errors (σ) in $km\,s^{-1}$. SNR denotes the signa-to-noise ratio around 5500Å wavelength.

TABLE 2

BEST-FITTING SPECTROSCOPIC ORBIT PARAMETERS OF KIC 4832197.[*]

Parameter	Value
P_{orb} (day)	1.8954655 (fixed)
T_0 (HJD24 00000+)	54954.965798 (fixed)
V_γ ($km\,s^{-1}$)	-41 ± 2
K_1 ($km\,s^{-1}$)	104 ± 4
K_2 ($km\,s^{-1}$)	113 ± 5
e	0 (fixed)
$a \sin i$ ($R_\odot$)	8.15 ± 0.26
$M \sin^3 i$ ($M_\odot$)	2.03 ± 0.14
Mass ratio ($q = M_2/M_1$)	0.92 ± 0.06
rms1 ($km\,s^{-1}$)	5
rms2 ($km\,s^{-1}$)	4

[*]M_1 and M_2 denote the masses of the primary and the secondary component, respectively, while M shows the total mass of the system and $a \sin i$ is the projected semi-major axis, depending on the orbital inclination i.

estimated temperature of the primary component and the overall metallicity are adopted as fixed parameters, and combined light curve and radial velocity modelling is repeated. Two or three iterations are usually enough to reach a self-consistent solution.

Effective temperatures and overall metallicity are estimated by the spectrum synthesis method. AT-LAS9 (Castelli & Kurucz 2004) model atmospheres, which adopt a plane-parallel atmosphere, are used for synthetic spectrum computation. A grid of synthetic spectra is computed for a temperature range of 6000 K to 7000 K with a step of 100 K. This computation is repeated for metallicities between solar ([Fe/H]=0) and sub-solar ([Fe/H]=−1.0), with a step of 0.25. The computation of synthetic spectra is done by a PYTHON framework, *iSpec* software (Blanco-Cuaresma et al. 2014). Among various radiative transfer codes provided in *iSpec*, the SPECTRUM code (Gray & Corbally 1994) is adopted. *iSpec* also includes a comprehensive line list compiled from the third version of the Vienna atomic line database (VALD3, Ryabchikova et al. 2015). Each computed synthetic spectrum is convolved with a Gaussian line spread function to reduce the spectral resolution to the resolution of the TFOSC spectra. After that, a trial synthetic spectrum is chosen for each component among the computed spectra, and a composite spectrum of the system is computed. In order to compute the composite spectrum of the system, each individual spectrum is shifted in wavelength with respect to the radial velocity of the corresponding component and scaled with respect to the square of the ratio of the radii of the components.

Self-consistent effective temperatures and overall metallicities are determined in the third iteration, which gives $T_{eff1} = 6300$ K, $T_{eff2} = 6100$ K and [Fe/H] $= -0.25$. The estimated uncertainties are around 200 K for temperature and 0.25 for metallicity. The adopted ratio of radii is $R_1/R_2 = 1.27$ and log g values are log $g_1 = 4.30$ and log $g_2 = 4.47$ (see next section for details). These results indicate F7V and F9V spectral types for the primary and the secondary components (Gray 2005), respectively. The observed TFOSC spectrum and the best-fitting composite spectrum are shown in Figure 5.
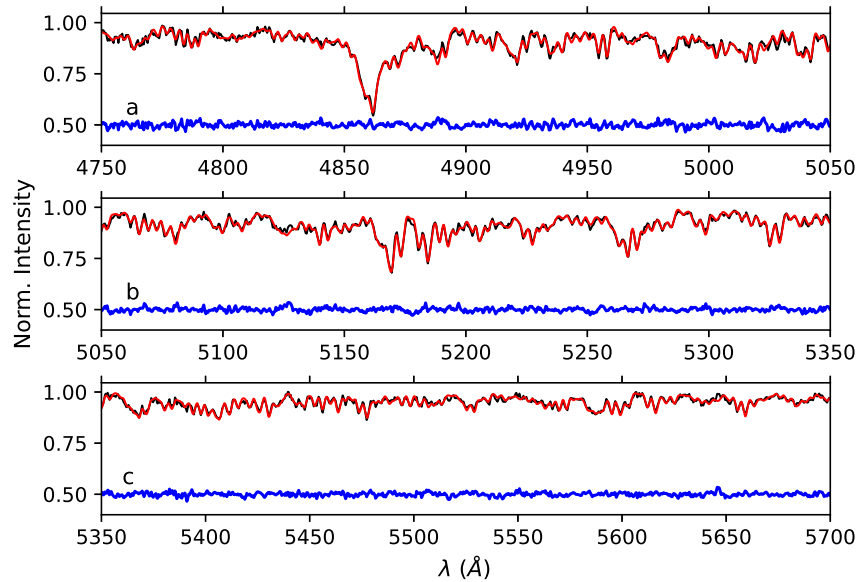
Fig. 5. Observed (blue) and computed composite spectrum (red) for KIC 4832197 in three different portions of the optical wavelengths. Residuals from the best-fitting model are plotted as shifted upwards by 0.5 (blue) for a better viewing purpose. The colour figure can be viewed online.

3.4. Light Curve Analysis and Evolutionary Status

Long cadence photometric data of KIC 4832197 include 65190 individual data points in total, which means that a large amount of CPU time is required to find a best-fitting light curve model. Therefore, an average phase-folded light curve is prepared by computing an average in every 0.01 phase at out-of eclipse phases. Around mid-eclipse phases a phase step of 0.0005 is adopted in order to detect the ingress and egress phases of eclipses precisely. The average phase-folded light curve includes 556 data points in total, which enormously reduces the required CPU time for light curve modelling. Weighting of each normal data point in the phase-folded average light curve is done by considering the total number of data points, which produces the normal data point.

Light curve modelling is done with the 2015 version of the well-known Wilson–Devinney (WD) eclipsing binary light curve modelling code (Wilson & Devinney 1971; Wilson & Van Hamme 2014). Its practical application is done by the user friendly PYTHON GUI $PyWD2015$ (Güzel & Özdarcan 2020). $PyWD2015$ allows the use of almost all features of the 2015 version of the WD code. In addition to the capabilities of the WD code, $PyWD2015$ includes many useful features and tools to speed up the modelling process and to trace successive iterations visually.

Two most critical parameters for an accurate light curve modelling are T_{eff1} and q. These have already been determined in previous sections, and are kept fixed during modelling. Effective temperatures of the components clearly indicate that both components possess a convective outer envelope; thus, gravity darkening (g) and albedo (A) values of each component are set to 0.32 (Lucy 1967) and 0.5 (Ruciński 1969), respectively. The low resolution of TFOSC spectra does not allow to determine reliable rotational velocities of the components; so, considering the non-eccentric orbit of the system, synchronous rotation is implicitly assumed for both components by fixing the rotation parameter (F) of each component to unity. A logarithmic limb darkening law (Klinglesmith & Sobieski 1970) is adopted for both components and limb darkening coefficients are taken from van Hamme (1993) for the Kepler passband. Adjustable parameters are: inclination of the orbit (i), effective temperature of the secondary component (T_{eff2}), dimensionless potentials of the components (Ω_1, Ω_2) and luminosity of the primary component (L_1). Coarse and fine grid numbers for the stellar surface are set to 60. Modelling attempts with a possible third light contribution do not yield a reasonable model, which indicates extremely small or negative third light contribution. Therefore, the modelling process is carried out with no third light contribution. Convergence is not very quick due to the shallow eclipse depths. However, successive it-
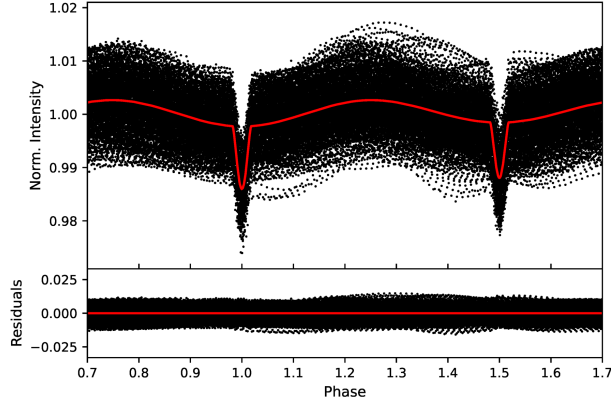
Fig. 6. Phase-folded long cadence Kepler observations and the best-fitting light curve model of KIC 4832197 are shown along with residuals from the model. The colour figure can be viewed online.

TABLE 3

BEST-FITTING LIGHT CURVE MODEL PARAMETERS FOR KIC 4832197.[*]

Parameter	Value
q	0.92 (fixed)
$T_1(K)$	6500 (fixed)
$g_1 = g_2$	0.32
$A_1 = A_2$	0.5
$F_1 = F_2$	1.0
i (°)	75.67(5)
$T_2(K)$	6060(200)
Ω_1	7.605(22)
Ω_2	8.520(44)
$L_1/(L_1+L_2)$	0.639(3)
x_1, x_2	0.685, 0.700
y_1, y_2	0.270, 0.259
$\langle r_1 \rangle, \langle r_2 \rangle$	0.1498(5), 0.1219(8)
Model rms	2.8×10^{-4}

[*]$\langle r_1 \rangle$ and $\langle r_2 \rangle$ show mean fractional radii of the primary and the secondary components, respectively. Uncertainties of the adjusted parameters are internal to the Wilson-Devinney code and are given in parentheses for the last digits, except T_2. The uncertainty of T_2 is assumed to be the same as that of T_1.

erations converge slowly but firmly to a global minimum. Model parameters for the best-fitting light curve are tabulated in Table 3. In Figure 6, the phase-folded light curve and and the best-fitting light curve model are shown. A separate close-up view of each eclipse is shown in Figure 7.

Combination of the best-fitting spectroscopic orbit and light curve model parameters allows us to compute the absolute dimension of the system as
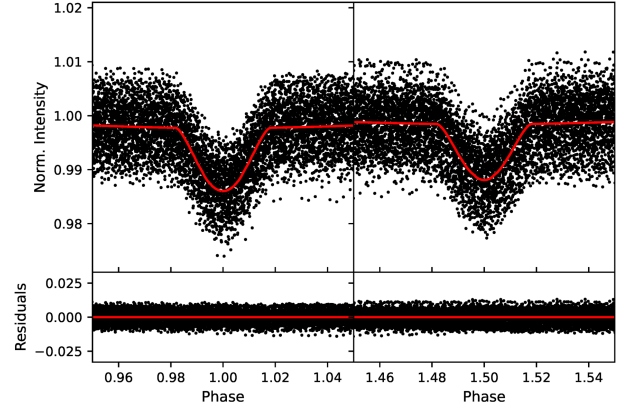

Fig. 7. Close-up view of observations and the best-fitting light curve model around eclipse phases. The colour figure can be viewed online.

TABLE 4

ABSOLUTE DIMENSION OF KIC 4832197.[*]

Parameter	Primary	Secondary
Spectral Type	F7V	F9V
Mass ($M_\odot$)	1.16(12)	1.07(10)
Radius ($R_\odot$)	1.26(4)	1.03(3)
$\log L/L_\odot$	0.35(6)	0.11(6)
$\log g$ (cgs)	4.30(2)	4.44(2)
M_{bol} (mag)	3.87(15)	4.48(16)
[Fe/H]	$-0.25(0.25)$	
Separation ($R_\odot$)	8.41(26)	
Distance (pc)	459(40)	

[*]The statistical error of each parameter is given in parentheses for the last digits.

well as its distance. Both the UBV colours (Everett et al. 2012) and the optical spectrum of the system indicate an F7 spectral type, which means that reddening and interstellar extinction should be negligible. Trial plotting of the system on the UBV colour-colour diagram gives $E(B-V) = 0.^{\mathrm{m}}009$, which is well below the observational error of $B-V$. Hence might be ignored for the distance computation. Considering P, K_1, K_2, i, $\langle r_1 \rangle$ and $\langle r_2 \rangle$ along with the published UBV magnitudes, the absolute dimension of the system is computed with the JKTABSDIM code[4] (Southworth et al. 2005) and tabulated in Table 4. Calibrations given in Kervella et al. (2004) are adopted for the bolometric correction and distance computation.

Comparing the locations of the components with stellar evolutionary tracks on the $\mathrm{Log}\, T_{eff} - \mathrm{Log}\, L/L_\odot$ plane, it is possible to es-

---

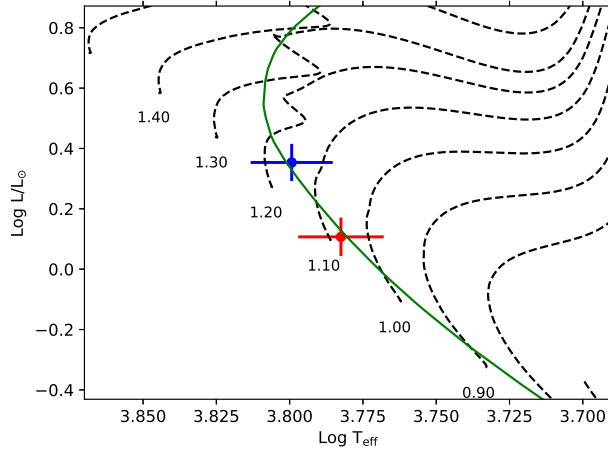[4]https://www.astro.keele.ac.uk/jkt/codes/jktabsdim.html

Fig. 8. Positions of the primary and the secondary components on $\log T_{eff} - \log L/L_{\odot}$ plane. Dashed lines show evolutionary tracks for different masses. Each track is labelled with its corresponding mass. The continuous curve shows the isochrone for $\log(age)=9.45$. The tracks are for a slightly sub-solar metallicity with $Y = 0.273$ and $Z = 0.014$. The colour figure can be viewed online.

timate the age of the system. In Figure 8, the components of KIC 4832197 are plotted along with stellar evolutionary tracks computed with the PAdova and TRieste Stellar Evolution Code (PARSEC, Bressan et al. 2012). The best-matching isochrone to the positions of the components has $\log(age)=9.45$, which indicates an age of 2.8 Gyr for the system. The estimated uncertainty for this age is approximately 0.8 Gyr. The primary source of this uncertainty is the uncertainty of the estimated effective temperatures and its propagation to the computed luminosities. Both components are still on the main sequence. However, the primary component is almost half-way through its main sequence life.

3.5. *Out-of-Eclipse Variability*

A scatter of ± 0.01 is clearly noticeable in the phase-folded light curve (see Figure 7). This scatter is a natural result of dominant brightness variability at out-of-eclipse phases (see Figure 1, lower panels). For further investigation of this variability, the best-fitting light curve model is subtracted from observations, and residuals from the model are obtained. In principle, these residuals do not include variability due to eclipses nor proximity effects of the components, and give hints on intrinsic variability of one or both components. Residuals from the best-fitting light curve model are obtained with PYWD2015 by inputting all long cadence data into

TABLE 5

FIRST TWO DOMINANT FREQUENCIES
$(F_1, F_2)^{*}$

Frequency number	Frequency (c/d)	Amplitude (Flux $\times 10^3$)	Phase (radian)
f_1	0.4995769(76)	3.70(2)	0.4947(8)
f_2	0.5339561(88)	2.79(2)	0.807(1)
f_{orb}	0.5275750(1)	—	—

[*]Resulting from the frequency analysis of the residual light curve of KIC 4832197 along with the orbital frequency (f_{orb}) of the system. Uncertainties are given in parentheses for the last digits.

the WD code and making a single differential corrections iteration. The obtained residuals are plotted in Figure 9. Quick changes in the residual light curve shape and amplitude are remarkable.

In order to see the reflection of this variability in the frequency-amplitude plane, a Lomb-Scargle periodogram (Lomb 1976; Scargle 1982) is applied to the whole long cadence residuals via a Python script PYSCA (Herzberg & Glogowski 2014). PYSCA allows quick and practical computation of the amplitude spectrum and can extract significant frequencies above a defined noise level. Adopting a 24.498 cycle/day (c/d) as Nyquist frequency, a single PYSCA run results in the amplitude spectrum given in Figure 10. The adopted Nyquist frequency corresponds to twice (≈ 59 min) the integration time of a single long cadence exposure. In the resulting amplitude spectrum, two dominant peaks are clearly seen around the orbital frequency, but no signal appears at the precise location of the orbital frequency. Frequency values of the two dominant peaks are tabulated in Table 5, together with the orbital frequency.

It is also possible to trace the behaviour of the detected frequency peaks for each Kepler quarter separately. A close view of the f_1 and f_2 peaks is shown in Figure 11 for each Kepler quarter, separately. It is apparent that f_1 strongly appears in most of quarters while f_2 weakens or disappears in some quarters.

The corresponding frequencies of the first two dominant peaks in the amplitude spectrum give the phase folded residual light curves shown in Figure 12. Phase folding is done with respect to the reference ephemeris given in equation 2 and the corresponding period values of the frequencies listed in Table 5. A wave-like light curve pattern can be noticed easily in both panels of the figure. This picture appears to be the reflection of a double-humped structure of the light curve (see Figure 1, Panels *b* and *c*), which is the frequently observed through four years of long
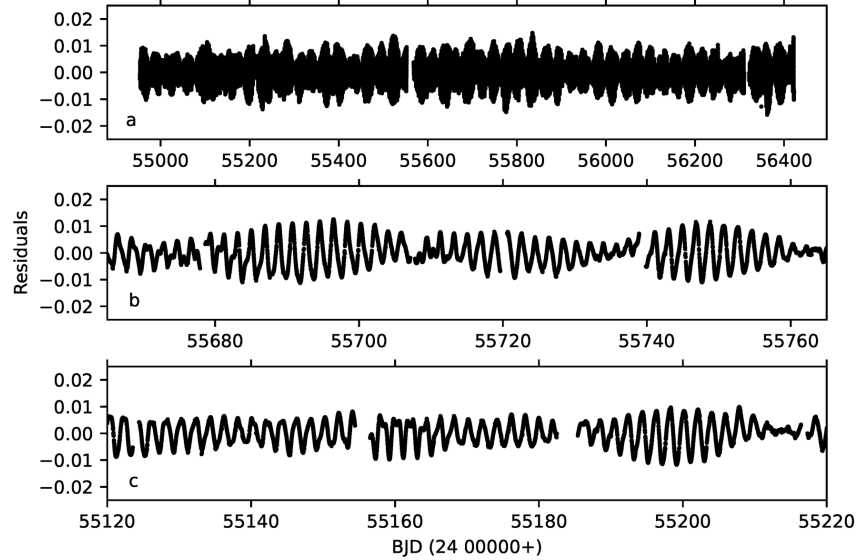
Fig. 9. Residuals from the best-fitting light curve model are plotted against time (BJD). Panel a shows the whole long cadence residuals, while Panels b and c show different portions of the whole set.
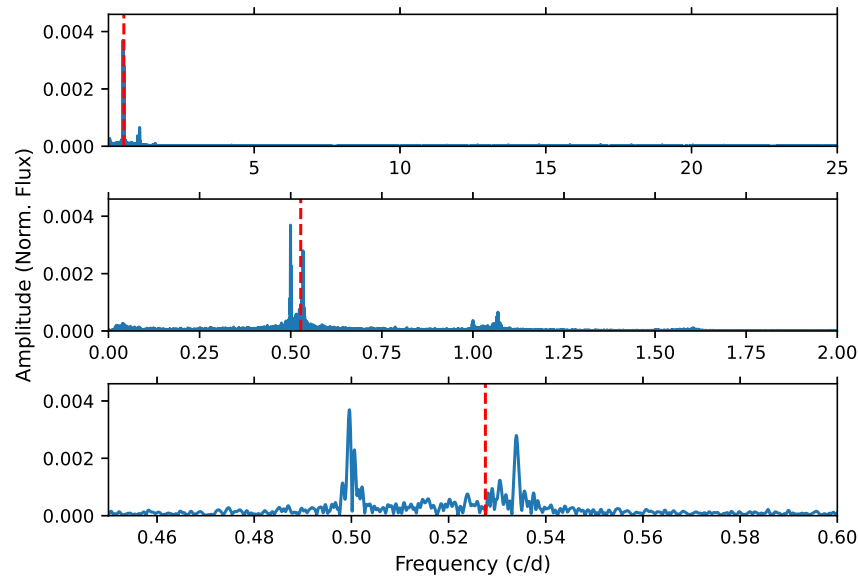

Fig. 10. Amplitude spectrum of light curve residuals. The uppermost panel shows the whole amplitude spectrum between 0 and 24.498 c/d. The middle panel focuses on 0 and 2 c/d, where dominant peaks appear. The lowermost panel shows a detailed view of the two most dominant peaks and the orbital frequency. In each panel, the orbital frequency is marked with a vertical dashed (red) line. The colour figure can be viewed online.

cadence data. Estimated spectral types of the components in § 3.3 suggest that these f_1 and f_2 frequencies are likely the result of cool spot activity on one or both components.

4. SUMMARY AND DISCUSSION

Analyses of medium resolution ground-based optical spectroscopy and very high precision Kepler photometry show that KIC 4832197 is composed of F7V and F9V stars possessing slightly sub-solar metallicity ([Fe/H]=-0.25 ± 0.25). The components move around the center-of-mass of the system in a circular orbit with a period of $1^\text{d}8954650$. The Kepler long cadence light curve of the system is dominated by a wave-like brightness variability whose amplitude is comparable to the eclipse depths. In some
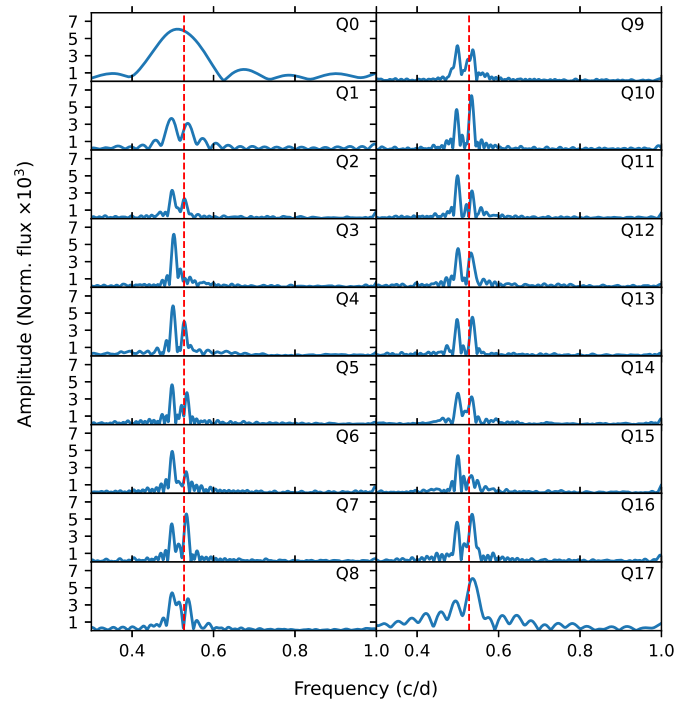
Fig. 11. Close view of the amplitude the spectrum of light curve residuals for each quarter of Kepler data. Panels are focused on the frequency region around f_{orb}, which is shown by a vertical (red) dashed line. Each panel is labelled with its corresponding quarter in the upper left corner. The colour figure can be viewed online.
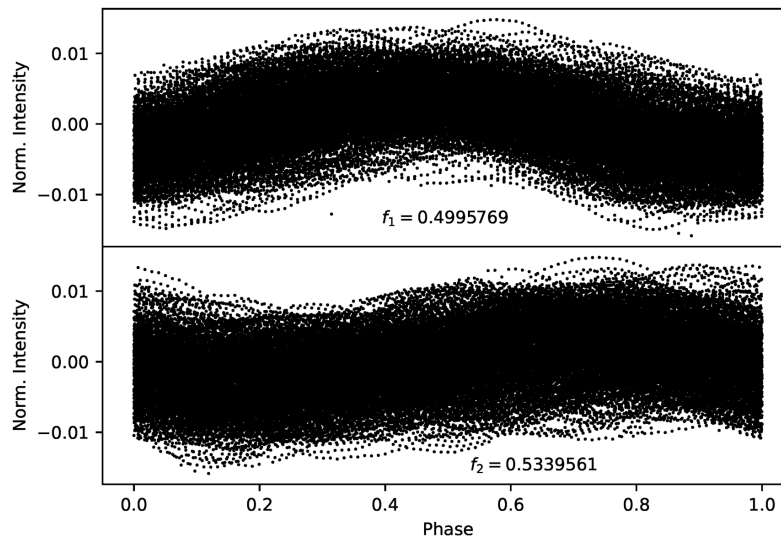

Fig. 12. Phase folded light curve residuals with respect to f_1 and f_2 frequencies. Each frequency is shown in the corresponding panel.

epochs, the amplitude of this variability exceeds the amplitude of eclipses, which are very shallow and hardly exceed 0.01 in normalized flux units.

Shallow eclipse depths could be result of a possible third light contribution. However, the best-fitting light curve model indicates no third light con-tribution. The ETV diagram does not show any sign for a possible third body, but only a scatter of ± 5 minutes with some vaguely undulating patterns among this scatter. A remaining possible explanation is that the undulating pattern could be the reflection of the variability observed at out-of-eclipse

phases. Considering the spectral types of the components, such irregular patterns in ETV diagrams could be attributed to an intrinsic photometric variability originating from magnetic activity of one or both components. (Balaji et al. 2015). Comparing the ETV diagrams of KIC 4832197 and a very active eclipsing binary KIC 12418816 (Dal & Özdarcan 2018, see Figure 1 in their study), it is clearly seen that our target system does not exhibit clear patterns, which indicates a much lower level of magnetic activity.

Combining the best-fitting spectroscopic orbit and light curve models, absolute physical properties of the components of the system are computed. Using these parameters, the components are plotted on the $\log T_{eff}$ − $\log L/L_{\odot}$ plane. The positions of the components on this plane suggest an age of 2.8±0.8 Gyr for the system. The primary component of KIC 4832197 appears to have burnt almost half of its main sequence fuel.

UBV colours (Everett et al. 2012) of the system enable us to estimate interstellar reddening. Trial plots of the $U − B$ and $B − V$ colours of the system on the UBV colour-colour diagram yields $E(B − V) = 0^{m}009$. This indicates a distance of 452±40 pc. Considering the reported observational errors of the UBV colours and the small amount of $E(B − V)$, interstellar reddening can be neglected. In this case, the distance becomes 459±40 pc. Both distance values agree within the computed statistical error. The computed error of the distance is mainly dominated by the estimated 200 K uncertainty of the effective temperatures of the components. The distance of the system based on precise parallax measurement of GAIA (Gaia Collaboration et al. 2016, 2022; Babusiaux et al. 2022) is given as 449±2 pc, which is in good agreement with the computed distance in this study.

Removing the best-fitting light curve model from the long cadence Kepler light curve, a residual light curve is obtained, which shows clear brightness variability at out-of-eclipse phases. The residual light curve exhibits remarkable changes, with a time scale of a few orbital cycles. These changes occur both in amplitude and shape of the light curves. For instance, an asymmetric single-humped light curve can become a double-humped one with a noticeable amplitude change in a few days, and then can return to another asymmetric light curve with a different amplitude. Considering the spectral types of the components the most likely explanation for the source of the out-of-eclipse brightness variability is cool spot activity on one or both components. Such a spot activity is the result of magnetic activity in cool stars and causes emission features to appear in particular activity-sensitive spectral lines throughout the optical spectrum (e.g. Hα, Ca II H& K lines). However, no emission features are observed, neither in the Hα nor in the Ca II H& K lines in the TFOSC spectra of KIC 4832197. Nevertheless, several very weak stellar flares, which can be considered photometric evidence of cool spot activity, are detected in the long cadence Kepler light curve of the system. Such a situation was observed before for the eclipsing binary KIC 9451096 (Özdarcan et al. 2018), where no emission was detected in activity-sensitive lines but a significant number of flares were detected in the Kepler light curve. On the other hand, although the amplitude of the rotational modulation signal reaches up to 0.01 in normalized flux units, this is still a low amplitude brightness variability. Thus, observing no emission in activity-sensitive spectral lines may not be unexpected. Actually, a low level of magnetic activity is in agreement with the physical properties of the system. Masses of the components are slightly higher than the solar mass, which means that both of them possess more shallow outer convective envelopes compared to the Sun. Therefore, one may expect a decrease in the level of magnetic activity. Comparing KIC 4832197 with KIC 12418816 (Dal & Özdarcan 2018), which is a lower mass eclipsing binary with shorter orbital period and high level of magnetic activity, confirms this situation. The components of KIC 12418816 possess a deeper convective envelope compared to the components of our target. As a result of the combination of faster rotation and deeper convective envelopes, a high level of magnetic activity in KIC 12418816 is not surprising. In the case of KIC 4832197, the situation is opposite. Hence, a low level of magnetic activity is not unexpected for KIC 4832198.

Frequency analysis of the residual light curve shows two dominant frequency peaks around the orbital frequency (see the amplitude spectrum plotted in Figure 10). However, the lowermost panel of the figure clearly shows that almost no signal appears at the exact location of the orbital frequency. This means that the best-fitting light curve model precisely represents binarity effects. As a result, removing the best-fitting light curve model from the observations perfectly removes the binarity effects from the long cadence light curve. Comparing the frequencies (f_1, f_2 and f_{orb}) and their statistical error (listed in Table 5), one can notice that the separation of frequencies exceeds the statistical errors. No major splitting is observed for the peaks of f_1

and f_2, except for a remarkable side component of f_1 located at a slightly higher frequency compared to f_1. We interpret these frequencies as the result of two separate spots or spot groups located at different latitudes on the surface of one or both components. Looking at the lowermost panel of the Figure 10, it is quickly seen that the f_1 and f_2 frequencies are smaller and larger than f_{orb}, respectively. Assuming that both components possess solar type differential rotation on their surfaces, a spot (or spot group) causing variability with an f_1 frequency is assumed to be located at lower latitudes, which are expected to rotate faster than at the latitude rotating with f_{orb}. (The latitude that rotates with f_{orb} is often called co-rotation latitude). In this case, the other spot (or spot group), which rotates with an f_2 frequency must be located at higher latitudes compared to the co-rotation latitude. These latitudes are expected to rotate slower than the co-rotation latitude as well. Further inspection of these frequencies reveals that f_1 persistently appears in each separate Kepler quarter while f_2 weakens or disappears occasionally. In this case, the spot (or spot group) related to f_1 is more persistent and exhibits stronger activity compared to the spot or spot group related to f_2. Four years of persistence of the f_1 frequency is not surprising in the context of solar and stellar activity since similar persistent active longitudes were reported previously for our Sun (Berdyugina & Usoskin 2003).

With the current data, it is difficult to distinguish which component possesses a spot(s) on its surface. However, we may make an implicit assumption by considering two mechanisms, depth of the outer convective envelope and rotation, which trigger the magnetic activity on cool stars. Although the system is composed of two similar stars, the secondary component is 500 K cooler than the primary. This means that the secondary star possesses a deeper convective envelope. Considering that the axial rotation periods of the components are synchronized with the orbital period, this finding indicates that the secondary component may exhibit stronger magnetic activity, because of its deeper convective outer envelope. Then, we may assume that the spots occur in the cool secondary component.

Assuming that both f_1 and f_2 come from spot or spot groups on the cool secondary component, a lower limit for the differential rotation can be set. Following the procedure described in Hall & Busby (1990), we compute the corresponding period for f_1 and f_2, and adopt them as minimum (P_{min}) and maximum (P_{max}) periods. Assuming a solar type

differential rotation, P_{min} can be adopted as the equatorial rotation period. Then, the relative surface shear can be computed via $P_{max} - P_{min}/P_{min} = kf$, where k is the differential rotation coefficient and f is a constant depending on the range of spot forming latitudes. Assuming that f varies between 0.5 and 0.7, which corresponds to 45 degrees of latitude range for spot forming, k varies between 0.14 and 0.10, which indicates an average $\bar{k} = 0.12$. This is half of the solar differential rotation coefficient ($k_\odot = 0.189$, see Hall & Busby (1990) and references therein) but twice the differential rotation coefficient of the eclipsing binary KIC 9451096 ($k = 0.069$, Özdarcan et al. 2018). This finding appears to contradict the theory of stellar magnetic activity since KIC 9451096 possesses a higher level of magnetic activity but a weaker differential rotation compared to our target system.

Increasing the number of precisely analysed solar type eclipsing binaries will provide a global look of the photometric properties of magnetic activity eclipsing binaries, and on the influence on light curves of differential rotation, which is one of the two key mechanisms responsible for magnetic activity in cool stars. Continuous photometric data provided by space telescopes is key to achieve this purpose.

REFERENCES

Babusiaux, C., Fabricius, C., Khanna, S., et al. 2022, arXiv e-prints, arXiv:2206.05989, https://doi.org/10.48550/arXiv.2206.05989

Balaji, B., Croll, B., Levine, A. M., & Rappaport, S. 2015, MNRAS, 448, 429, https://doi.org/10.1093/mnras/stv031

Balona, L. A. 2015, MNRAS, 447, 2714, https://doi.org/10.1093/mnras/stu2651

Berdyugina, S. V. & Usoskin, I. G. 2003, A&A, 405, 1121, https://doi.org/10.1051/0004-6361:20030748

Blackwell, D. E. & Shallis, M. J. 1979, MNRAS, 186, 673, https://doi.org/10.1093/mnras/186.4.673

Blanco-Cuaresma, S., Soubiran, C., Heiter, U., & Jofré, P. 2014, A&A, 569, 111, https://doi.org/10.1051/0004-6361/201423945

Borucki, W. J., Koch, D., Basri, G., et al. 2010, Sci, 327, 977, https://doi.org/10.1126/science.1185402

Bressan, A., Marigo, P., Girardi, L., et al. 2012, MNRAS, 427, 127, https://doi.org/10.1111/j.1365-2966.2012.21948.x

Castelli, F. & Kurucz, R. L. 2004, A&A, 419, 725, https://doi.org/10.1051/0004-6361:20040079

Coughlin, J. L., Mullally, F., Thompson, S. E., et al. 2016, ApJS, 224, 12, https://doi.org/10.3847/0067-0049/224/1/12

Dal, H. A. & Özdarcan, O. 2018, MNRAS, 474, 326, https://doi.org/10.1093/mnras/stx2875

Everett, M. E., Howell, S. B., & Kinemuchi, K. 2012, PASP, 124, 316, https://doi.org/10.1086/665529

Fitzpatrick, M. J. ASPC 52, Astronomical Data Analysis Software and Systems II, ed. R. J. Hanisch, R. J. V. Brissenden, & J. Barnes, 472

Gaia Collaboration, Prusti, T., de Bruijne, J. H. J., et al. 2016, A&A, 595, 1, https://doi.org/10.1051/0004-6361/201629272

Gaia Collaboration, Vallenari, A., Brown, A. G. A., et al. 2022, arXiv:2208.00211, https://doi.org/10.48550/arXiv.2208.00211

Gilliland, R. L., Jenkins, J. M., Borucki, W. J., et al. 2010, ApJ, 713, 160, https://doi.org/10.1088/2041-8205/713/2/L160

Gray, D. F. 2005, The Observation and Analysis of Stellar Photospheres, 3rd ed. (Cambridge, UK: CUP)

Gray, R. O. & Corbally, C. J. 1994, AJ, 107, 742, https://doi.org/10.1086/116893

Güzel, O. & Özdarcan, O. 2020, CoSka, 50, 535, https://doi.org/10.31577/caosp.2020.50.2.535

Hall, D. S. & Busby, M. R. 1990, ASIC 319, Proceedings of the NATO Advanced Study Institute on Active Close Binaries, ed. C. Ibanoglu, 377

Henry, G. W. & Eaton, J. A. 1995, ASPC 79, Robotic telescopes: current capabilities, present developments, and future prospects for automated astronomy: proceedings of a symposium held as part of the 106th annual meeting of the Astronomical Society of the Pacific, Arizona, 28-30 June 1994

Herzberg, W. & Glogowski, K. 2014, IAUS, Precision Asteroseismology, 421, https://doi.org/10.1017/S1743921313014853

Høg, E., Fabricius, C., Makarov, V. V., et al. 2000, A&A, 355, 27

Howell, S. B., Sobeck, C., Haas, M., et al. 2014, PASP, 126, 398, https://doi.org/10.1086/676406

Kervella, P., Thévenin, F., Di Folco, E., & Ségransan, D. 2004, A&A, 426, 297, https://doi.org/10.1051/0004-6361:20035930

Klinglesmith, D. A. & Sobieski, S. 1970, AJ, 75, 175, https://doi.org/10.1086/110960

Kochanek, C. S., Shappee, B. J., Stanek, K. Z., et al. 2017, PASP, 129, 104502, https://doi.org/10.1088/1538-3873/aa80d9

Kwee, K. K. & van Woerden, H. 1956, BAN, 12, 327

Landstreet, J. D., Kupka, F., Ford, H. A., et al. 2009, A&A, 503, 973, https://doi.org/10.1051/0004-6361/200912083

Lomb, N. R. 1976, Ap&SS, 39, 447, https://doi.org/10.1007/BF00648343

Lucy, L. B. 1967, ZA, 65, 89

Özdarcan, O. & Dal, H. A. 2017, PASA, 34, 17, https://doi.org/10.1017/pasa.2017.11

Özdarcan, O., Yoldaş, E., & Dal, H. A. 2018, RMxAA, 54, 37, https://doi.org/10.48550/arXiv.1709.01129

Pojmanski, G. 1997, AcA, 47, 467, https://doi.org/10.48550/arXiv.astro-ph/9712146

Prugniel, P., Vauglin, I., & Koleva, M. 2011, A&A, 531, 165, https://doi.org/10.1051/0004-6361/201116769

Prša, A., Batalha, N., Slawson, R. W., et al. 2011, AJ, 141, 83, https://doi.org/10.1088/0004-6256/141/3/83

Reinhold, T. & Gizon, L. 2015, A&A, 583, 65, https://doi.org/10.1051/0004-6361/201526216

Rodonò, M., Cutispoto, G., Lanza, A. F., & Messina, S. 2001, AN, 322, 333, https://doi.org/10.1002/1521-3994(200112)322:5/6<333::AID-ASNA333>3.0.CO;2-6

Ruciński, S. M. 1969, AcA, 19, 245

Ryabchikova, T., Piskunov, N., Kurucz, R. L., et al. 2015, PhyS, 90, 054005, https://doi.org/10.1088/0031-8949/90/5/054005

Scargle, J. D. 1982, ApJ, 263, 835, https://doi.org/10.1086/160554

Slawson, R. W., Prša, A., Welsh, W. F., et al. 2011, AJ, 142, 160, https://doi.org/10.1088/0004-6256/142/5/160

Southworth, J., Maxted, P. F. L., & Smalley, B. 2005, A&A, 429, 645, https://doi.org/10.1051/0004-6361:20041867

Strassmeier, K. G., Boyd, L. J., Epand, D. H., & Granzer, T. 1997, PASP, 109, 697, https://doi.org/10.1086/133934

Tonry, J. & Davis, M. 1979, AJ, 84, 1511, https://doi.org/10.1086/112569

van Hamme, W. 1993, AJ, 106, 2096, https://doi.org/10.1086/116788

Wilson, R. E. & Devinney, E. J. 1971, ApJ, 166, 605, https://doi.org/10.1086/150986

Wilson, R. E. & Van Hamme, W. 2014, ApJ, 780, 151, https://doi.org/10.1088/0004-637x/780/2/151

Yoldaş, E. & Dal, H. A. 2021, RMxAA, 57, 335, https://doi.org/10.22201/ia.01851101p.2021.57.02.07

H. A. Dal, O. Özdarcan, and E. Yoldaş: Ege University, Faculty of Sciences, Department of Astronomy and Space Sciences, 35100 Bornova, İzmir, Turkey (orkun.ozdarcan@ege.edu.tr).